Limnol. Oceanogr., 50(5), 2005, 1601–1611
© 2005, by the American Society of Limnology and Oceanography, Inc.

Interbasin exchange and mixing in the hypolimnion of a large lake: The role of long internal waves

Lars Umlauf
Baltic Sea Research Institute, Seestrasse 15, D-18119 Rostock, Germany

Ulrich Lemmin
Laboratoire d'Hydraulique Environnementale, Faculté ENAC, EPFL, CH-1015 Lausanne, Switzerland

Abstract

We conducted a combined field and numerical study of the effects of episodic internal Kelvin-type waves on bottom boundary turbulence and the exchange of a passive tracer between the main basin and the side basin of a large lake (Lake Geneva). High-resolution measurements of the vertical current structure near the entrance of the 25-km-long and 70-m-deep side basin revealed that hypolimnetic current speeds frequently exceed 0.2 m s^{-1}, leading to a turbulent bottom boundary layer several meters thick with logarithmic current profiles and to a region of strong shear across the thermocline. The time series and vertical structure of the currents were reproduced by a three-dimensional numerical model of the lake. It was demonstrated that, after episodes of strong winds from the northeast and southwest, exchange flows due to internal Kelvin waves were able to temporarily half or double the hypolimnetic volume of the side basin, leading to an irreversible exchange of up to 40% of the hypolimnetic water in the side basin of Lake Geneva within only a few wave cycles. With the help of the numerical model, it was shown that the key mechanisms of exchange are horizontal dispersion by resolved scales and, to a small extent, shear dispersion in the bottom boundary layer. It is suggested that bottom boundary-layer turbulence and the interbasin exchange can explain the structural differences in the oxygen profiles observed in the side basin and the main basin, respectively.

Past hydrodynamic studies conducted in Lake Geneva (Fig. 1a) present a consistent picture of a lake dominated by the presence of several modes of wind-forced long internal waves modified by the Earth's rotation (Mortimer 1974; Bäuerle 1985; Lemmin et al. 2005) and by a broad spectrum of short internal waves (Thorpe et al. 1996; Thorpe and Lemmin 1999; Thorpe and Umlauf 2002). The occurrence of long internal waves, most notably internal Kelvin-type and Poincaré-type waves, is a typical and well-known feature also observed in other lakes of comparable size and has been documented in numerous field studies and numerical experiments (Umlauf et al. 1999; Rueda et al. 2003; Appt et al. 2004).

The present work concentrates on the role of internal Kelvin-type waves on the exchange of matter between the main basin of a lake and its smaller and shallower side basin, taking Lake Geneva as an example. We will demonstrate that this type of interbasin exchange has physics distinct from the basin-wide residual- and direct-transport patterns described by other authors (Ou and Bennet 1979; Strub and Powell 1986; Lemmin and D'Adamo 1996). Using field observations and a numerical model, the first objective of this article is to illustrate how episodic events of enhanced Kelvin wave activity lead to a strong net transport between the side basin and the main basin. Second, we will demonstrate that Kelvin-type waves in Lake Geneva lead to a turbulent bottom boundary layer (BBL) in the side basin, with a thickness of several meters and turbulence levels comparable with those in the upper mixing layer under strong winds. As recently pointed out by Lorke et al. (2003), the presence of such a BBL is of considerable importance for the hypolimnetic oxygen budget because it may completely control the flux of oxygen through the viscous sublayer into the sediment. Additionally, the existence of a turbulent BBL with strong vertical velocity gradients and high diffusivities suggests that shear dispersion may be an important mechanism.

Previous modeling studies of long interval wave motions in large lakes were either purely numerical in nature (e.g., Beletsky et al. 1997; Umlauf et al. 1999) or compared model results with the thermal signatures of internal waves (Hodges et al. 2000; Pan et al. 2002; Appt et al. 2004). Lemckert et al. (2004) studied velocity profiles derived from a microstructure probe in a turbulent BBL induced by basin-scale internal waves but did not attempt to compare their results with a numerical model. In the context of long interval waves in large and deep lakes, surprisingly, we only found one direct comparison of results from a three-dimensional model with currents, which were, however, measured at a single depth and with low temporal resolution (Rueda et al. 2003). It appears that a comparison of three-dimensional model results and measurements of high-resolution vertical

Acknowledgment

We thank Steve Thorpe for making valuable suggestions for the improvement of an earlier version of this manuscript. We are also indebted to Claude Perrinjaquet for the excellent technical support and to the Commision Internationale pour la Protection des Eaux du Léman' (CIPEL) for providing some of the data. We also thank the two anonymous reviewers for many helpful suggestions and remarks.

Part of this work was carried out within the framework of the project EUROLAKES (EU-contract EVK1-CT1999-00004) sponsored by the Swiss Federal Office of Science and Research (contract 99.0190). We are grateful for the support.

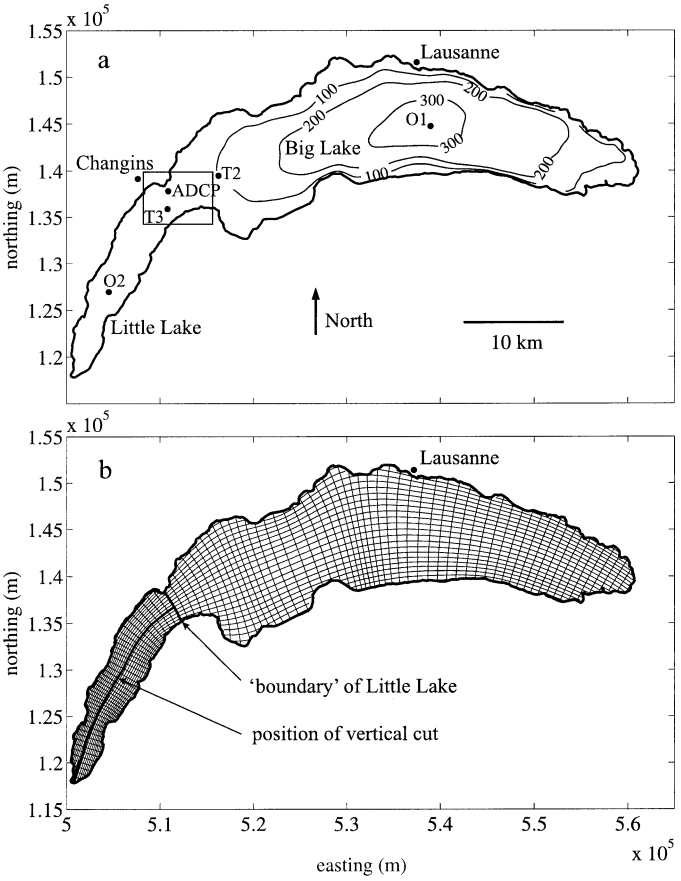

Fig. 1. (a) Topography of Lake Geneva with the two subbasins, Big Lake (main basin) and Little Lake (side basin). T2 and T3 denote measuring stations for high-resolution temperature profiles, O1 and O2 for oxygen profiles and low resolution temperature profiles. ADCP indicates the position of two acoustic profilers. Meteorological data were obtained from Sta. Changins. (b) Curvilinear numerical grid (thin lines); for clarity, only every third grid line is displayed. Thick grid lines define the boundary of the side basin and the vertical plane for along-basin plots shown below.

current profiles induced by long interval waves in a lake and a combined field and model study of the interbasin exchange due to such waves has not yet been carried out.

Lake Geneva

Lake Geneva is Western Europe's largest lake, situated at approximately 47°N in the prealpine region at the border between Switzerland and France. It consists of a 310-m-deep main basin, called the Grand Lac (Big Lake), and a smaller side basin of about 25 km length and 4 km width, called the Petit Lac (Little Lake) (see Fig. 1a). We use a grid line of the curvilinear numerical grid discussed in detail below to define the open boundary between the two basins of Lake Geneva (see Fig. 1b).

During the summer/fall season (May–October), both basins of Lake Geneva are strongly stratified with a pronounced thermocline between 15 and 30 m depth. In late fall, the thermocline weakens considerably and usually descends down to a depth of 80–100 m in winter (January–March). The side basin, with a maximum depth of approximately 75 m, is almost entirely mixed during parts of the cold season. Complete mixing of the main basin has rarely been observed (CIPEL 2003). Maximum temperatures in the epilimnion during summer range from 18°C to 24°C, whereas the temperature in the lower hypolimnion of the large basin is between 5.5°C and 6°C. Density stratification by salinity and suspended sediment plays a negligible role for the overall dynamics of Lake Geneva. River inflow is relatively small, resulting in a theoretical residence time of 12 years. Two very small rivers discharge into the side basin. Their effect on hydrodynamics and water quality can be neglected.

The wind field over Lake Geneva during summertime has been carefully analyzed by Lemmin and D'Adamo (1996). These authors pointed out the existence of two typical winds over Lake Geneva resulting from meso-scale atmospheric forcing, modified by the particular topography around the lake. These winds are much stronger than the lake–land breeze but are observed only occasionally during the stratified season. The first of these winds comes from the northeast and is called the Bise, the second, referred to as Vent, blows from the southwest. Both winds are confined by the blocking effects of the Alps in the southeast and the Jura mountains in the northwest (Lemmin and D'Adamo 1996). Given the geometry of the surrounding topography, both winds have a long fetch and can generate considerable currents in the Lake. Lemmin and D'Adamo (1996) and Lemmin et al. (2005) pointed out that, when studying long interval waves, it is reasonable to consider the Bise and the Vent as spatially homogeneous winds. Therefore, in the present study, we will restrict our attention to those hydrodynamic processes resulting from the fairly homogeneous Bise and Vent. The wind records of the Swiss Meteorological Service from the Sta. Changins (less than 2 km from the lake shore; see Fig. 1a) will be used in our calculations. If Bise and Vent dominate, this station is representative for the whole lake, except for the easternmost part.

The numerical model

Shallow-water model—The three-dimensional numerical model used in our study is based on the Reynolds averaged Navier–Stokes equations with the Boussinesq and shallow-water approximations invoked. The temperature equation is solved simultaneously. Models based on these equations have been shown to compare reasonably well with time series of measured flow properties as well as with the low wave-number part of measured spectra (Laval et al. 2003; Rueda et al. 2003; Appt et al. 2004).

In addition to the shallow-water equations, an equation for a conserved passive scalar,

$$\frac{\partial c}{\partial t} + u\frac{\partial c}{\partial x} + v\frac{\partial c}{\partial y} + w\frac{\partial c}{\partial z} - \frac{\partial}{\partial z}\left[(\nu^c + \nu_t^c)\frac{\partial c}{\partial z}\right] - D_H^c = 0 \quad (1)$$

has been solved. Here, u, v, and w denote the velocities in the coordinate directions x, y, and z, respectively. The effects of vertical molecular and turbulent transport are expressed in terms of the molecular and vertical turbulent diffusivities

of the tracer, v^c and v_t^c, respectively. The subgrid horizontal transport of c is denoted by D_H^c. Because no specific tracer is considered in this study, we assume, for simplicity, that the diffusivities of the tracer are identical to that of heat. The governing equations for this type of model are discussed, for example, by Haidvogel and Beckmann (1999). The model used to compute the vertical turbulent diffusivities is explained below.

The numerical code is described in detail in Burchard and Bolding (2002). It uses a horizontal curvilinear Arakawa C grid with 300 × 70 grid points, approximately following the shoreline of Lake Geneva. We used the flexibility of the curvilinear coordinate system to achieve locally varying grid spacing with a resolution comparable with the maximum water depth in both basins (Fig. 1b). This high-resolution grid is computationally demanding because a well-known stability criterion requires that a time step of 1 s for the barotropic mode and 120 s for the internal mode be chosen in order to assure stability of the explicit, total variation diminishing (TVD) advection scheme. The vertical grid corresponds to a generalized topography-following (sigma-type) coordinate system with 80 vertical layers and a refined vertical resolution near the sediment (grid zooming; see Burchard and Bolding, 2002). With this technique, the vertical grid spacing in the turbulent BBL of the 70-m-deep side basin is less than 0.5 m, and thus sufficient to resolve the observed logarithmic velocity profiles (see below). The resolution of the turbulent BBL is of fundamental importance for the correct representation of mixing and sediment–water fluxes of momentum and matter. Note that a Cartesian vertical grid requires more than 600 vertical layers for a comparable vertical resolution of the BBL in the side basin because the depth of the main basin is 310 m.

Turbulence model

The vertical turbulent transport of momentum and heat is computed from a so-called explicit algebraic stress model (EASM), resulting from a reduced form of the second-moment transport equations for the turbulent fluxes. Canuto et al. (2001) showed that, by neglecting the third-moment transport terms and the rate terms in those equations, the vertical diffusivities of momentum and heat for that type of model could be expressed in the form $\nu_t = c_\mu(S, Fr_t)k^{1/2}l$, where k denotes the turbulent kinetic energy and $l \propto k^{3/2}\varepsilon^{-1}$ the dissipative length scale, computed from the rate of dissipation, ε. The stability function, c_μ, depends on the nondimensional shear-number, $S = Mk^{-1/2}l$, and the turbulent Froude number, $\mathrm{Fr}_t = N^{-1}k^{1/2}l^{-1}$, where $M = ((\partial u/\partial z)^2 + (\partial v/\partial z)^2)^{1/2}$ is the shear frequency and N the buoyancy frequency. Details and model parameters are discussed by Canuto et al. (2001), and a comparison of this and other models for marine turbulence can be found in Burchard and Bolding (2001).

The turbulent kinetic energy is prognostically computed from its transport equation, and the dissipation rate $\varepsilon \propto k\omega$ is assumed to be proportional to k and the turbulent frequency, ω, where the latter quantity results from a parameterized transport equation (Umlauf and Burchard 2003; Umlauf et al. 2003). Boundary conditions for mean and turbulent quantities were derived by assuming that the logarithmic law of the wall is always valid between the sediment and the lowest grid point (see Burchard and Bolding 2002).

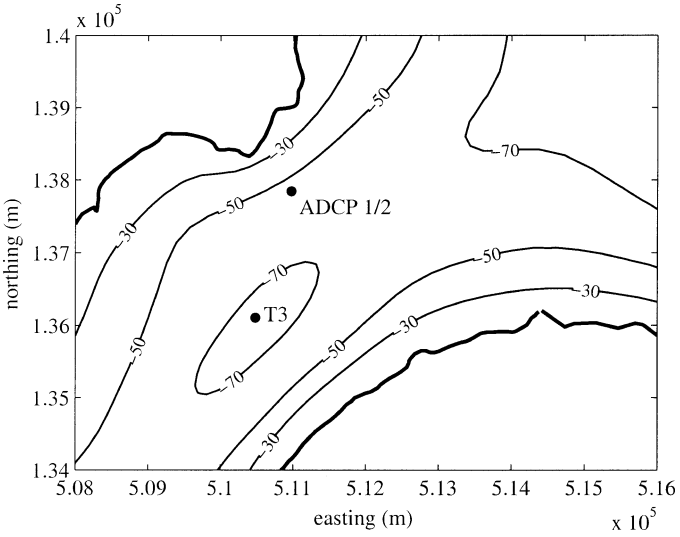

Fig. 2. Detailed view of the topography at the entrance region of the side basin; see Fig. 1. ADCP1/2 indicates the location of the two ADCPs, T3 the position where high-resolution temperature profiles were taken. Depth contours are given in meters.

The most important properties of this turbulence model can be summarized as follows. The model (i) has been thoroughly tested in a large number of unstratified flow cases and shown to be superior to other two-equation models, such as the k-ε model (Wilcox 1998), (ii) does not require any wall functions to predict turbulent quantities in the law of the wall (Wilcox 1998), (iii) computes correct mixing efficiencies in stably stratified shear flows (Canuto et al. 2001), (iv) is in excellent agreement with experimental data for mixed layer deepening by surface-wind stress (Umlauf et al. 2003, 2005), and (v) predicts the correct height of a shear-driven turbulent BBL and correct dissipation rates within the BBL (Lorke et al. 2002; Umlauf et al. 2005).

Field data

Routine measurements of coarse-resolution temperature and oxygen profiles are conducted once or twice a month in the center of the main basin and the side basin at Sta. O1 and O2 by the CIPEL (2003) (see Fig. 1a). In addition, we took high-resolution temperature profiles during the years 1986–1992 near station O1 at the deepest point and at Sta. T2 and T3 near the entrance of the side basin (see Figs. 1, 2).

A representative stratification profile for the month of September, the month of our measuring campaign, is depicted in Fig. 3. This profile corresponds to the high-resolution profile measured on 12 September 1989 at T1 in the main basin, and exhibits the smallest root mean square error with respect to the mean from all available profiles in September. From this profile, an internal first-mode Rossby-radius of approximately 4 km can be estimated. Also shown in Fig. 3 is the

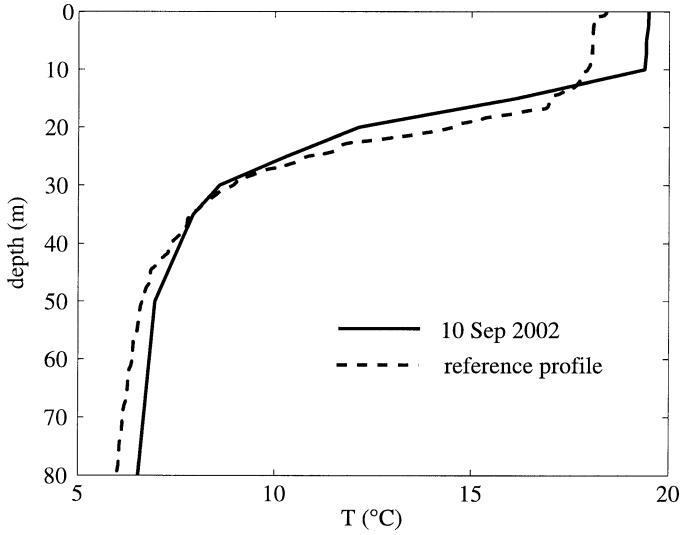

Fig. 3. Temperature profiles measured at Sta. O1 in the main basin on 10 September 2002 and 12 September 1989. The latter is a representative profile, exhibiting the lowest root mean square error with respect to the mean of all measured profiles in September over all years.

temperature profile on 10 September 2002, before the wind event discussed in this article.

Figure 4 shows oxygen profiles routinely measured at Sta. O1 and O2 every September for the decade from 1992 to 2002 (see Fig. 1). Profiles measured in the main basin for this period in late summer (Fig. 4a) exhibit a characteristic structure repeated every year. The most pronounced features in these profiles are a metalimnetic oxygen minimum with a peak at about 20–30 m depth and a strong oxygen deficit in the lower hypolimnion, where concentrations near the bottom are close to zero. This structure is also observed in other deep alpine lakes of similar trophic level and has been discussed, e.g., for Lake Constance by Wagner and Kruse (1995) and for Lake Ammer by Joehnk and Umlauf (2001). These authors pointed out that, for this class of lakes, the oxygen deficit in the lower hypolimnion is predominantly controlled by the sedimentary oxygen demand (SOD).

Profiles measured on the same dates at Sta. O2 in the side basin exhibit a substantially different structure (Fig. 4b). Measured hypolimnetic oxygen concentrations are very similar to those in the same depth range at Sta. O1 in the main basin, but no oxygen deficit in the hypolimnion is visible. This is rather unexpected because production and sedimentation are similar and SOD in the side basin should be of the same order as that in the main basin. Moreover, the ratio of sediment surface to hypolimnetic volume, a critical parameter for the effect of SOD on the hypolimnetic oxygen deficit, is approximately nine times larger in the side basin than in the main basin. In view of these findings and the strong vertical density stratification, it is surprising that no hypolimnetic oxygen deficit at all is found near the bottom of the side basin. This fact motivated the idea that oxygen concentrations in the side basin are controlled by a strong horizontal exchange with the main basin.

In order to study the spatial and temporal variation of the

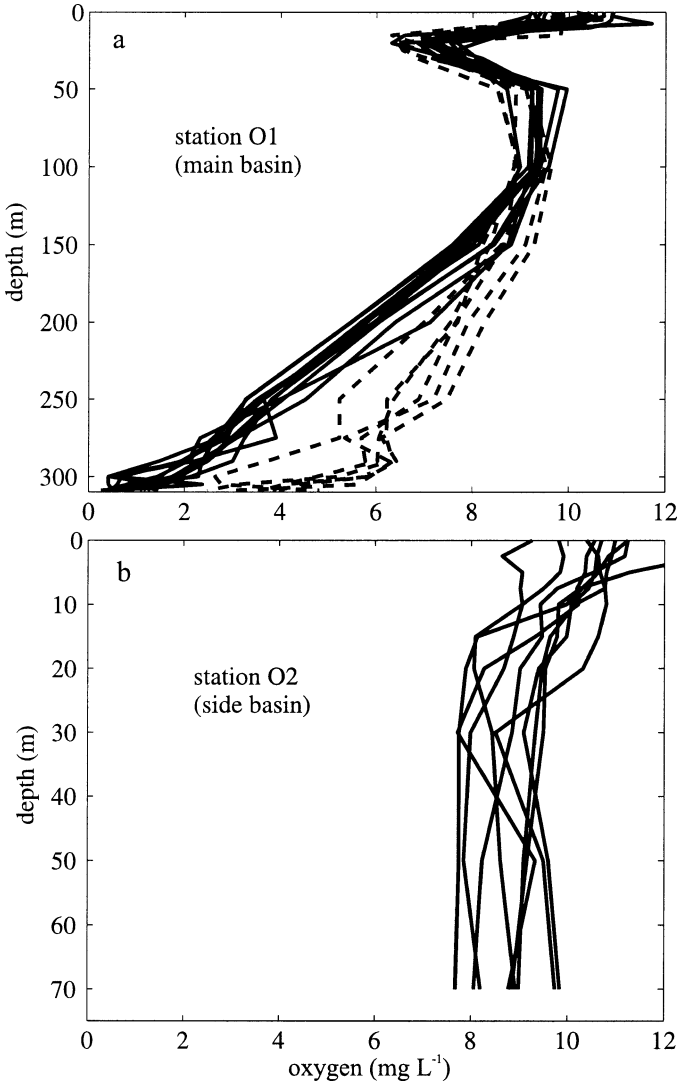

Fig. 4. Oxygen concentration for September 1992–2002 at (a) Sta. O1 in the main basin and (b) Sta. O2 in the side basin. Dashed lines in (a) correspond to profiles measured after February 1999, when partial overturning occurred in Lake Geneva.

exchange flows between the two basins of Lake Geneva and to investigate the dynamics of the turbulent BBL, vertical current profiles were measured at the entrance of the side basin at Sta. ADCP1/2 (Fig. 2). For a period of approximately 7 weeks from 06 September until 17 October 2002 (days 249–290), two acoustic Doppler current profilers (ADCPs) with different vertical resolution and bin size were mounted on a heavy platform, which was placed on the sediment at a depth of about 54 m. The platform was installed at a location relatively close to the northern shore (Fig. 2), where currents produced by internal Kelvin-type waves coming from the main basin and traveling along the northern shore into the side basin were expected to be most pronounced.

ADCP 1 was an RD Instruments profiler operating with 50 bins of 1 m size, the lowest bin being centered at 5.15 m above the sediment. This instrument allowed us to resolve

current profiles throughout the water column except for the uppermost 4 m, where the signal was strongly affected by backscattering from the water surface. ADCP 2 was a Nortek Aquadopp profiler operating with 10 bins of 0.5-m size. The head of the Aquadopp profiler is side looking, which allowed us to locate the center of the lowest bin at only 0.65 m above the sediment. The purpose of this instrument was to provide a detailed description of the velocity structure of the BBL. Both ADCPs where synchronized to record currents averaged over 5 min. The ping rate was set to reduce the instrument-induced standard deviation to less than 0.01 m s^{-1}. Because we were only interested in low-frequency variations, the current data were low-pass filtered with a cut-off period of 60 min.

The evaluation of the current records at ADCP 1 indicated that directions of inflow and outflow are topographically constrained to a small angle range around 35 degrees for outflow and 215 degrees for inflow into the side basin. This corresponds approximately to the basin axis near the entrance region (Fig. 2). Therefore, all data obtained from the ADCPs have been projected onto this plane using the convention that outflow from the side basin is to be taken as positive.

Velocity time series and vertical current structure

The period during which vertical current profiles were recorded included a strong wind event corresponding to one of the most typical wind fields over Lake Geneva, the Bise from the northeast (Lemmin and D'Adamo 1996). Because this wind event was preceded by a calm weather period of more than 1 week with very low wind speeds from variable directions, an almost ideal starting point was given for studying the effect of episodic wind events on the long interval wave field.

The Bise event

The period from 23 September to 01 October 2002 (days 266–274) was characterized by an event with wind speeds reaching up to 10 m s^{-1} from the northeast at the meteorological station at Changins (Fig. 5a,b). Figure 5c,d presents the projected current speeds from ADCP 1 at representative levels in the epilimnion and the hypolimnion, respectively. Model results, also shown in this figure, will be discussed below. The displayed time period starts with a strong wind from the northeast, which pushes epilimnetic water into the side basin on day 267 and the beginning of day 268, whereas conservation of mass requires that hypolimnetic water leaves it. Current speeds reach 0.25 m s^{-1} in the hypolimnion during this initial phase. After the collapse of the first wind pulse on day 268, a current reversal is observed at ADCP 1. From day 268 to day 270.5, the wind speed is low. Thereafter, it again increases to more than 5 m s^{-1}, until breakdown of the wind on day 272 (Fig. 5a). Thus, the second wind pulse is approximately in phase with the surface current, providing additional energy input into the oscillating current and leading to even higher current velocities in the epilimnion.

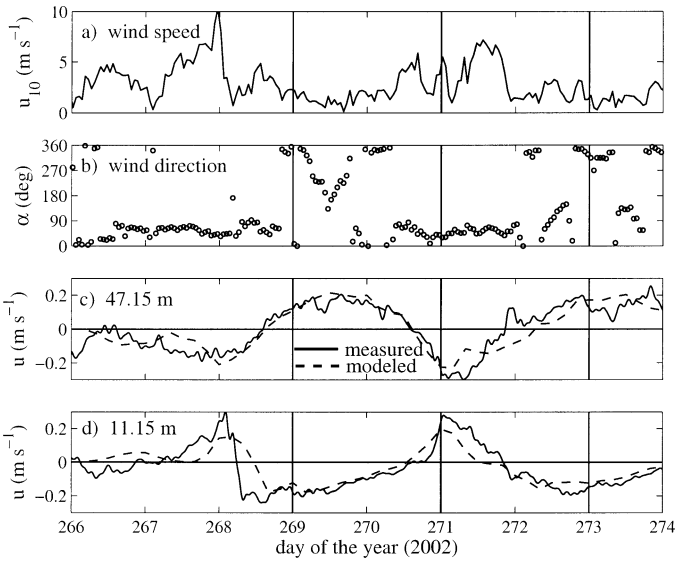

Fig. 5. Wind data for days 266–274 in 2002: (a) wind speed and (b) wind direction at Changins. Measured and modeled currents at ADCP 1: (c) at 47.15 m above the bottom and (d) at 11.15 m above the bottom. Local water depth is 54 m, currents are projected onto a vertical plane rotated 35 degrees from the north. Flow toward the main basin is positive. Vertical lines indicate specific times for current profiles displayed in Fig. 6.

The oscillation of the current has a clear physical interpretation in terms of an internal Kelvin wave traveling cyclonically around the basin. The observed period of slightly more than 3 d is in good agreement with the numerical analysis of Lake Geneva's eigenmodes and a variety of measurements (Mortimer 1963; Bäuerle 1985; Lemmin et al. 2005). Manifestations of internal Kelvin waves were also clearly visible in our three-dimensional model results, e.g., as strong thermocline excursions and velocity signals traveling counterclockwise along the shoreline (not shown).

Vertical profiles of horizontal currents at selected times indicated in Fig. 5 are displayed in Fig. 6. The upper 4 m of the water column are not shown because acoustic backscatter disturbed the velocity data from ADCP 1 close to the free surface. The selected days, 269, 271, and 273, correspond to phases of high current speeds in the epi- and hypolimnion during the wave cycle. Figure 6 supports the classical current pattern of a first vertical mode internal wave, with currents in the upper layer driven by the barotropic pressure gradient and currents in the lower layer by the baroclinic pressure gradient. It should be noted that the shear across the central region of the profiles can be quite substantial (see, for example, day 271 in Fig. 6), possibly leading to instabilities of the Kelvin–Helmholtz type. The profiles in Fig. 6 also exhibit some evidence of friction effects because all profiles show the onset of a BBL at their lower end. This aspect of the flow will be investigated in the following section with the help of the high-resolution data from ADCP 2 in the turbulent BBL.

Turbulent bottom boundary layer

The lower parts of the profiles in Fig. 6 suggest that, close to the sediment, the flow is affected by bottom friction and

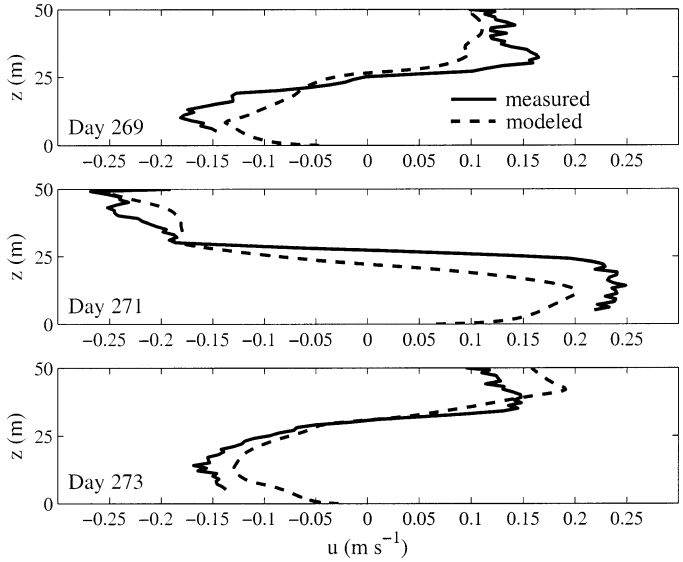

Fig. 6. Measured and modeled current profiles for the times indicated in Fig. 5. Local water depth is 54 m. Note that the upper 4 m are not displayed (acoustic backscatter).

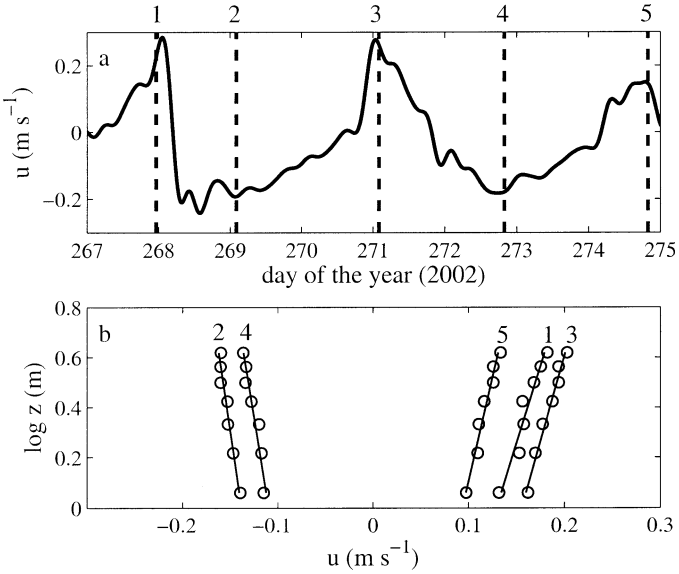

Fig. 7. Plotted for days 267–275 in 2002: (a) speed 11.15 m above bottom, (b) data (circles) and logarithmic fits at the times indicated by dashed lines in (a). Note the numbering of the profiles.

that a turbulent BBL may have developed. To investigate this point further, data from ADCP 2, resolving the lowest 5 m of the water column with bins of 0.5-m vertical extent, were evaluated. The measured profiles were therefore fitted to the logarithmic boundary layer expression,

$$\frac{u}{u_*} = \frac{1}{\kappa} \ln \frac{z}{z_0} \tag{2}$$

where κ denotes the von Kármán constant, u_* the friction velocity, and z_0 the bottom roughness length. The latter two quantities are obtained from the slope and the abscissa intersection of the fitted profiles. The results of these curve fits at selected times during the Bise event (Fig. 5) are displayed in Fig. 7. When the current speed is high, the fit is satisfactory, confirming the idea of a logarithmic BBL extending over at least $10^{0.6} \approx 4$ m above the sediment. Above this level, the law of the wall may break down (see Fig. 6). As would be expected, the fit is less satisfactory during low speeds, in particular during flow reversal (not shown).

Numerical results

The numerical model was driven with winds measured by the Swiss Meteorological Service at the Sta. Changins (Fig. 1a) for days 266–274. Because winds were low and variable for more than a week before day 266, residual currents from previous wind events were small and model results become comparable with the data after a short spin-up time. As explained above, the Sta. Changins can be considered representative for the purpose of this study. The sensitivity of model results to variations of the wind field is discussed below.

Apart from the empirical formulas for the meteorological fluxes (see Burchard and Bolding, 2002), the only free model parameter is the bottom roughness length which was set to $z_0 = 0.01$ m, a value suggested by the results of the logarithmic fits in the BBL (see above). The model was initialized with zero velocities and with the temperature profile from 10 September 2002 (Fig. 3).

Comparison with modeled currents

The analysis of the model results revealed two major oscillations dominating the internal wave field: the first one consists of superinertial standing Poincaré-type waves with periods between 10 and 12 h in the main basin. The second one is the first vertical-mode Kelvin-type wave traveling counterclockwise along the shore of the lake with a period of approximately 3 d. The appearance of these internal waves in Lake Geneva is well-documented and agrees with earlier analyses of Bäuerle (1985) and Lemmin et al. (2005).

The internal Kelvin-type wave dominates the currents near the entrance of the side basin. Modeled and measured time series of the currents at ADCP 1 in the hypolimnion and the epilimnion are compared in Fig. 5c,d. Close agreement during the first 2 d, when velocities were low, cannot be expected because the numerical model started from rest. After day 268, however, the model reproduces the speed and phase of the internal oscillation in both layers with good agreement. In the lower layer, the model slightly underestimates the maximum velocities.

The current profiles on days 269, 271, and 273 (Fig. 6) again show good agreement between the measured and modeled vertical current structure. A more detailed examination of the model results corroborates that the observed strong currents at the entrance are associated with incoming Kelvin waves from the main basin. Kelvin waves are reflected at the end of the side basin and decay exponentially away from the shore. It is worth pointing out that, in combination with the modifications of the currents due to the distorted topography near the entrance, this leads to a highly variable ver-

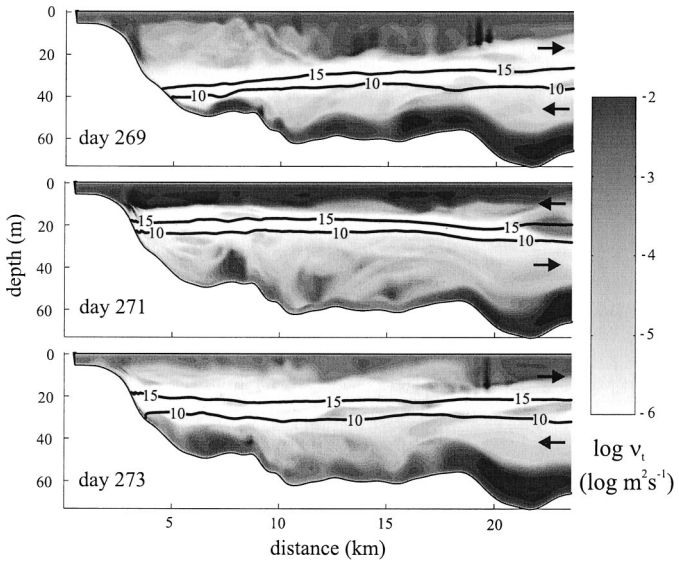

Fig. 8. Vertical transect (see Fig. 1b) of modeled turbulent diffusivity along the side basin for days 269, 271, and 273 in 2002. Arrows illustrate in- and outflow across the entrance, black contour lines at 10°C and 15°C mark the thermocline region. Distance corresponds to arc length along the vertical transect (Fig. 1b).

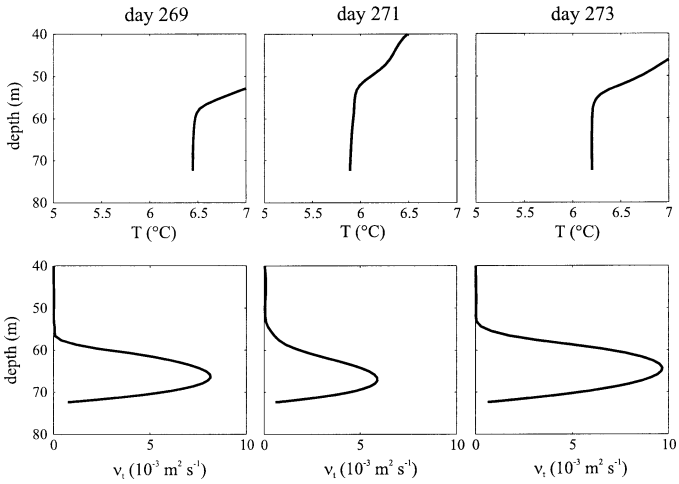

Fig. 9. Modeled temperature and diffusivity profiles at Sta. T3 for days 269, 271, and 273 in 2002.

tical structure of inflow and outflow events across the entrance region. Thus, the reproduction of the observed current profiles at ADCP 1 is a stringent test for the quality of any numerical model.

Vertical transects through the side basin along the grid plane indicated in Fig. 1b are presented in Fig. 8. The contours of the modeled turbulent diffusivity and the 10°C and 15°C isotherms indicating the thermocline region are shown for days 269, 271, and 273, corresponding to the profiles in Fig. 6. Note that the Kelvin-wave–induced exchange currents cause large thermocline excursion in the side basin. It can be seen that both surface and bottom stress lead to pronounced turbulent boundary layers with turbulent diffusivities up to $\nu_t = 10^{-2}$ m^2 s^{-1}. This is in contrast with the thermocline region, where turbulence is strongly suppressed by stable stratification and turbulent diffusivities range between $\nu_t = 10^{-6}$ and 10^{-5} m^2 s^{-1}. These are typical values for thermocline and boundary layer turbulence in lakes with strong wind forcing (Wüest and Lorke 2003). Figure 8 shows that enhanced turbulence in the BBL is predicted throughout the side basin with greatest thickness and intensity of the turbulent BBL near the entrance, where hypolimnetic velocities are highest. The location and the vertical extent of the turbulent BBL are in agreement with the logarithmic velocity profiles shown in Fig. 7.

Modeled vertical profiles of temperature and turbulent diffusivity for days 269, 271, and 273 at Sta. T3 in the side basin near the entrance (see Fig. 1a) are compiled in Fig. 9. These results clearly indicate that the model predicts a turbulent BBL with nearly homogeneous temperature profiles in all cases, topped by the strong temperature gradient in the thermocline. The lower row in Fig. 9 demonstrates that the vertical extent of the BBL is consistent with enhanced values of the turbulent diffusivity. Recalling the high hypolimnetic velocities and the strong velocity shear due to the law of the wall in the BBL (Fig. 7b), these results suggest that vertical shear dispersion in the entrance region could be an important mechanism determining the mixing of water masses between the main basin and the side basin.

Evidence for the existence of strong BBL mixing at Sta. T3 comes from an older set of temperature observations presented in Fig. 10. High-resolution temperature profiles were available for late summer (August and September) during the years 1986–1992 at Sta. T2 in the main basin and T3 in the side basin, located on either side of the open boundary (see Fig. 1a). At both stations, profiles are displayed for the depth range 40–80 m, which includes the lower hypolimnion of the side basin. Corresponding profiles at the two locations were taken on the same days with a maximum delay of 60 min. The persistent temperature gradient at T2 in the main basin, typical for the upper hypolimnion of Lake Geneva, is strongly contrasted by the existence of a rather well-mixed BBL at T3 in the side basin. The vertical extent and the vertical structure of the profiles at the latter station are in qualitative agreement with the modeled profiles displayed in Fig. 9. These data, taken at random dates, indicate that a well-mixed BBL at T3 is the rule rather than the exception.

Interbasin exchange

A sketch of the principal processes relevant to the renewal of hypolimnetic water in the side basin of a large lake is given in Fig. 11. The hypolimnetic volume, $V(t)$, is defined by the volume of water with a temperature below a certain threshold, taken here to be 10°C (see Fig. 3). $V(t)$ can be changed by reversible motion of the bounding isothermal surface, i.e., by thermocline excursion, as well as by irreversible displacement of the isothermal surface caused by diapycnal mixing (V_{mix} in Fig. 11). The total volume change with respect to the initial volume is $\Delta V(t)$. The balance of mass in an incompressible fluid requires that the reversible part of $\Delta V(t)$ must be balanced by the time-integrated volume flux through the open boundary with the main basin,

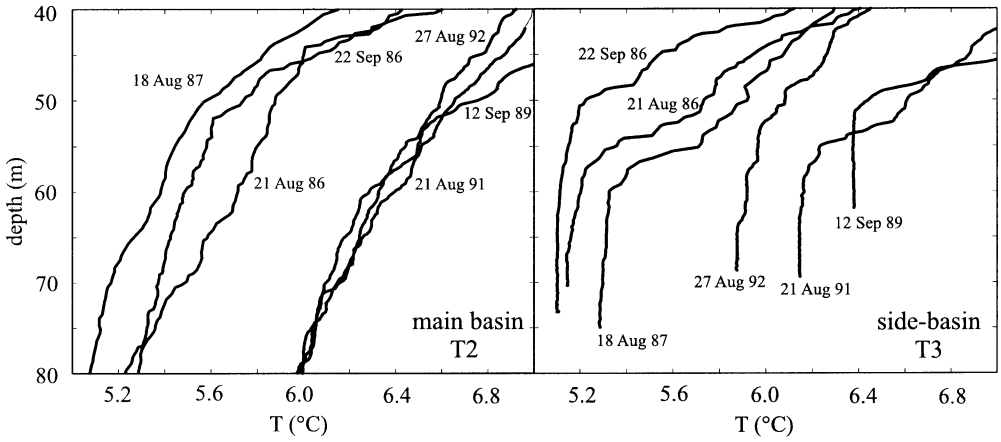

Fig. 10. Hypolimnetic temperature profiles (a) at T2 in the main basin and (b) at T3, the side basin, measured over several years in August and September (see Fig. 1a). Dates as indicated.

$-V_{out}$. The budget of a passive tracer can be developed in a similar way, except for the fact that reversible volume changes, evidently, do not change the total tracer mass. The extent to which water is renewed depends on how the outflowing tracer mass, M_{out}, is advected away from the entrance and/or mixed with water of different tracer concentration in the main basin. Similarly, the inflowing tracer from the main basin, $-M_{out}$, is dispersed and internally mixed with water from the side basin. These are the key processes determining the water renewal in the side basin.

Idealized cases

We numerically investigated the tracer exchange between the main basin and the hypolimnion of the side basin. The initial stratification corresponded to the representative profile of 12 September 1989 (Fig. 3). The hypolimnion of the side basin was marked by a passive tracer of concentration 1 and zero tracer flux from or to the sediment. Because we were interested in the exchange between the two basins, the tracer concentration in the main basin was set to zero.

The subgrid scale horizontal transport in Eq. 1 was set to $D_H^c = 0$ for the following reasons: First, we wanted to avoid the application of the commonly used Fickian diffusion models, which are known to have a rather weak theoretical basis and require diffusion coefficients that are not precisely known. Setting $D_H^c = 0$ implies that all our results represent lower bounds for the interbasin exchange. Second, the numerical grid near the entrance region is very fine. Therefore, it can be expected that a large fraction of the total horizontal dispersion is performed by resolved scales. Resolved-scale dispersion can be reliably estimated because it does not require any modeling assumptions.

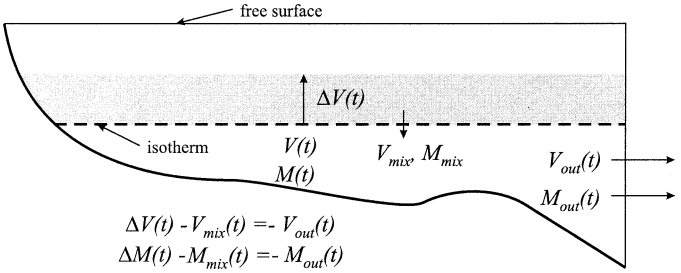

Fig. 11. Sketch of volume and mass fluxes for the hypolimnion of the side basin. The vertical line to the right indicates the open boundary with the main basin (see Fig. 1b). The grey-shaded area marks the total volume change of the hypolimnion, $\Delta V(t)$, caused by vertical motion of the isothermal surface (thermocline).

The temporal evolution of the total tracer concentration and the tracer exchange with the main basin was studied for several patterns of the typical wind fields Vent from the southwest and Bise from the northeast. For both directions, the surface wind stress was linearly increased to its maximum value, τ_{max}, during the first day, then left unchanged during the second day, after which it was set to zero for the rest of the run. The scenario was considered to be a simple representation of a typical strong wind event on Lake Geneva. Different temporal variations of the wind stress, e.g., without linearly increasing stress during the first day, yielded similar results, provided the time-integrated momentum flux was identical. Varying the wind directions by 20 degrees around northeast and southwest (larger variations are unlikely due to topographical constraints) changed the results presented in the following by less than 10%. We also investigated the possible effect of the wind stress curl by tapering off the wind in the easternmost part, as suggested by Lemmin et al. (2005). This only produced small variations of the results. We found, in accordance with Lemmin et al. (2005), that the structure of the Kelvin waves in the entrance region is not sensitive with respect to the spatial structure of the wind field supplying energy and momentum to these waves.

In contrast with the wind-field orientation, the magnitude of the wind stress was found to be an important factor. We investigated the effects of weak, intermediate, and strong maximum surface stresses, setting $\tau_{max} = 0.05$, $\tau_{max} = 0.1$, and $\tau_{max} = 0.15$ Pa, respectively. With the quadratic friction law used in the numerical model, these correspond to wind speeds of 5.2, 7.3, and 9.0 m s^{-1}, respectively. These values approximately span the range of maximum wind speeds during the northeasterly winds displayed in Fig. 5a,b.

Shown in Fig. 12 a,b are modeled time series of the vol-

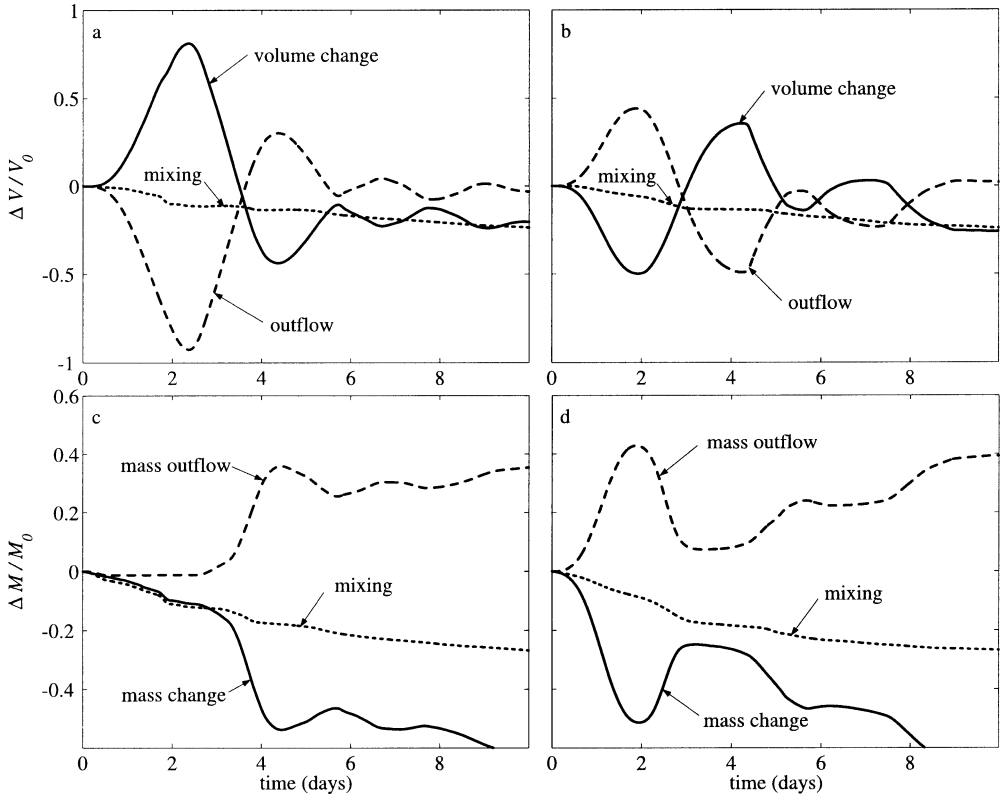

Fig. 12. Budget of the hypolimnetic volume and tracer mass in the side basin. (a) Volume change with respect to initial volume, integrated outflow toward main basin, and mixing across 10°C isotherm for the Vent from the southwest and (b) same for the Bise from the northeast; (c) and (d) the same as (a) and (b), but now for tracer mass. For details, see text.

ume change, $\Delta V(t)$, the time-integrated outflow, $V_{out}(t)$, of hypolimnetic water from the side basin, and irreversible volume changes due to mixing, $V_{mix}(t)$ (see Fig. 11). All quantities have been nondimensionalized by the initial hypolimnetic volume, V_0. Because the overall dynamics are qualitatively similar for the three wind-stress cases, only the case of intermediate wind stress, with $\tau_{max} = 0.1$ Pa is discussed in detail. The effect of varying the wind stress is discussed below.

It is evident from Fig. 12a,b that, for both wind fields, $\Delta V(t)$ is balanced to first order by the oscillating outflow, $V_{out}(t)$, which clearly shows the signature of Kelvin waves. The contribution due to mixing, $V_{mix}(t)$ is seen to be a second-order effect resulting in a loss of hypolimnetic volume due to mixing, causing a gradual lowering of the 10°C isotherm. We observed in the model results that the mixing contribution is the sum of several processes related to boundary mixing, entrainment, and upwelling near the shoreline. For the Vent from the southwest shown in Fig. 12a, inflowing hypolimnetic water from the main basin has nearly doubled the initial volume of the hypolimnion of the side basin on day 2.3; for the Bise from the northeast in Fig. 12b, the hypolimnion has lost more than 40% of volume on day 1.9. Compared with these values, the volume loss caused by diapycnal mixing is relatively small, but not negligible. Thus, the most important observation from these simulations is that internal Kelvin waves provide for the exchange of a considerable fraction of the hypolimnetic water between the two basins. Note that large thermocline excursions, and thus large volume changes, are also evident from the realistic run (see Fig. 8). The question is to what extent these exchange flows are irreversible.

The fundamental difference between volume and tracer exchange is illustrated in Fig. 12c,d, showing the budget of the tracer mass, nondimensionalized by the initial tracer mass in the side basin, M_0. For the Vent from the southwest, fresh water from the main basin with zero tracer concentration enters the hypolimnion of the side basin until day 2.3 (see Fig. 12a), leaving the total tracer mass in the hypolimnion almost unchanged. During the outflow phase on days 2.3–4.2 (Fig. 12a), approximately 35% of the initial tracer mass is advected out of the hypolimnion of the side basin into the main basin. After flow reversal, inflow due to the internal wave motion on days 4.2–5.8 causes only a small portion of this tracer mass to be advected back into the side basin. This fact clearly illustrates the irreversible nature of the exchange process due to resolved-scale dispersion, leading to a large net exchange of tracer between the subbasins on a short time scale. It can be seen from Fig. 12d that, apart from the different timing, similar processes take place for the Bise wind field from the northeast. As mentioned above, only resolved-scale dispersion has been considered in this study. The effect of the ignored subgrid scale dispersion would lead to even larger exchange rates.

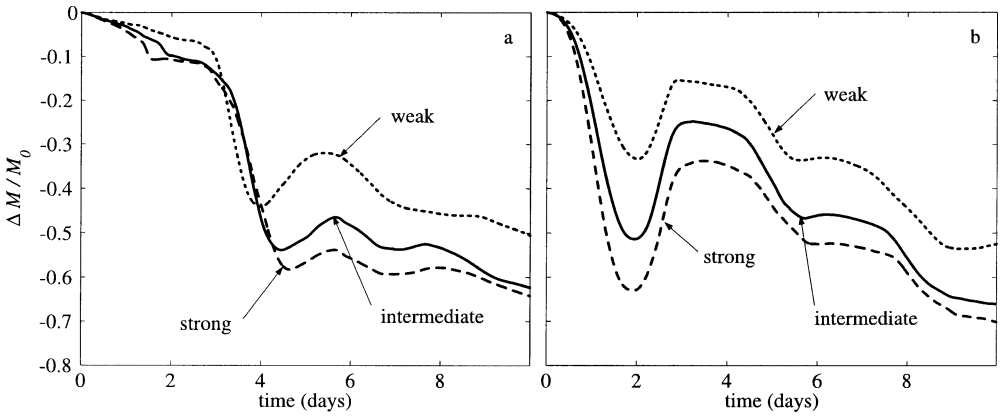

Fig. 13. Time series of total tracer mass in the side basin for different wind stresses (a) for the Vent from the southwest and (b) for the Bise from the northeast.

We also isolated the effect of vertical shear dispersion by comparing a standard run (with the vertical turbulent diffusivities of the tracer computed from the turbulence model), with a run with zero vertical tracer diffusivity, $\nu_t^c = 0$, and thus no shear dispersion. Because the tracer is passive, this has no influence on the other fields. It was found that, for both wind directions, vertical shear dispersion accounts for less than 10% of the total irreversible exchange.

Figure 13 illustrates the effect of variations of the strength of the wind stress on the total tracer mass in the hypolimnion of the side basin. It is evident from this figure that, for both wind directions, varying the wind stress does not change the qualitative picture of the exchange process. However, tracer exchange is seen to be a nonlinear function of the wind stress. It is particularly evident that very strong winds only slightly increase the tracer exchange. Recalling the low sensitivity of model results with respect to changes in wind direction, temporal variation, and wind stress curl, this implies that model results for intermediate wind speeds provide a representative estimate for the interbasin exchange due to episodic internal Kelvin waves.

It is evident that these results have strong implications for the dynamics of biogeochemical parameters in the side basin (see Fig. 4). The suggested exchange process can, for example, explain the absence of a hypolimnetic oxygen minimum in the side basin. The occurrence of a turbulent BBL is also chemically relevant; Lorke et al. (2003) pointed out that such turbulent boundary layers are of crucial importance for the oxygen transport through the viscous sublayer toward the sediment

Our results are likely to be applicable to other large lakes with a well-defined side basin. For example, recent studies on Lake Constance, Western Europe's second largest lake, revealed that Kelvin-type waves after wind events may lead to strong (several 10s of meters) vertical thermocline excursions in the Lake of Überlingen, an elongated side basin of Lake Constance with a similar geometry as the side basin of Lake Geneva (Appt et al. 2004). Even though these authors did not directly measure current speeds, their simulations clearly show that, after strong wind events, the observed thermocline excursions in the side basin imply strong exchange currents with the main basin of Lake Constance.

References

APPT, J., J. IMBERGER, AND H. KOBUS. 2004. Basin-scale motion in stratified Upper Lake Constance. Limnol. Oceanogr. **49:** 919–93.

BÄUERLE, E. 1985. Internal free oscillations in the Lake of Geneva. Ann. Geophysicae **3:** 199–206.

BELETSKY, D., W. P. O'CONNOR, D. J. SCHWAB, AND D. E. DIETRICH. 1997. Numerical simulation of internal Kelvin waves and coastal upwelling fronts. J. Phys. Oceanogr. **27:** 1197–1215.

BURCHARD, H., AND K. BOLDING. 2002. GETM—a general estuarine transport model. Technical Report EUR 20253 EN. European Commission.

———, AND ———. 2001. Comparative analysis of four second-moment turbulence models for the oceanic mixed layer. J. Phys. Oceanogr. **31:** 1943–1968.

CANUTO, V. M., A. HOWARD, Y. CHENG, AND M. S. DUBOVIKOV. 2001. Ocean turbulence, Part I: One-point closure model—momentum and heat vertical diffusivities. J. Phys. Oceanogr. **31:** 1413–1426.

CIPEL. 2003. Rapports sur les études et recherches entreprises dans le bassin Lémanique; programme quinquennal 2001–2005; campagne 2002. Obtainable from: Commission internationale pour la protection des eaux du lac Léman (www.cipel.org), Lausanne 12, Switzerland.

HAIDVOGEL, D. B., AND A. BECKMANN. 1999. Numerical ocean circulation modelling, v. 2 of Series on Environmental Science and Management. Imperial College Press London.

HODGES, B. R., J. IMBERGER, A. SAGGIO, AND K. WINTERS. 2000. Modeling basin-scale internal waves in a stratified lake. Limnol. Oceanogr. **45:** 1603–1620.

JOEHNK, K. D., AND L. UMLAUF. 2001. Modelling the metalimnetic oxygen minimum in a medium sized alpine lake. Ecol. Model. **136:** 67–80.

LAVAL, B., J. IMBERGER, B. HODGES, AND R. STOCKER. 2003. Modeling circulation in lakes: Spatial and temporal variations. Limnol. Oceanogr. **48:** 983–994.

LEMCKERT, C., J. ANTENUCCI, A. SAGGIO, AND J. IMBERGER. 2004. Physical properties of turbulent benthic boundary layers generated by internal waves. J. Hydr. Eng. **130:** 58–69.

LEMMIN, U., AND N. D'ADAMO. 1996. Summertime winds and direct cyclonic circulation: Observations from Lake Geneva. Ann. Geophysicae **14:** 1207–1220.

———, C. H. MORTIMER, AND E. BÄUERLE. 2005. Internal seiche dynamics in Lake Geneva. Limnol. Oceanogr. **50:** 207–216.

LORKE, A., L. UMLAUF, T. JONAS, AND A. WÜEST. 2002. Dynamics of turbulence in low-speed oscillating bottom-boundary layers of stratified basins. Environ. Fluid Mech. **2:** 291–313.

———, B. MÜLLER, M. MAERKI, AND A. WÜEST. 2003. Breathing sediments: The control of diffusive transport across the sediment-water interface by periodic boundary-layer turbulence. Limnol. Oceanogr. **48:** 2077–2085.

MORTIMER, C. H. 1963. Frontiers in physical limnology with particular reference to long internal waves in rotating basins. Proceedings of the 5th Conference of the Great Lakes Research Division, Univ. Michigan, 9–42.

———. 1974. Lake hydrodynamics. Mitt. Int. Ver. Theor. Angew. Limnol. **20:** 124–197.

OU, H. W., AND J. R. BENNET. 1979. A theory of the mean flow driven by long internal waves in a rotating basin, with application to Lake Kinneret. J. Phys. Oceanogr. **9:** 1112–1125.

PAN, H., R. AVISSAR, AND D. B. HAIDVOGEL. 2002. Summer circulation and temperature structure of Lake Kinneret. J. Phys. Oceangr. **32:** 295–313.

RUEDA, F. J., S. G. SCHLADOW, AND S. O. PALMARSSON. 2003. Basin-scale internal wave dynamics during a winter cooling period in a large lake. J. Geophys. Res. **108:** 3097, doi: 10.1029/2001JC000942.

STRUB, P. T., AND T. M. POWELL. 1986. Wind-driven surface transport in stratified closed basins: Direct versus residual circulation. J. Geophys. Res. **91:** 8497–8508.

THORPE, S. A., J. M. KEEN, R. JIAN, AND U. LEMMIN. 1996. High frequency internal waves in Lake Geneva. Phil. Trans. R. Soc. Lond. A **354:** 237–257.

———, AND U. LEMMIN. 1999. Internal waves and temperature fronts on slopes. Ann. Geophys. **17:** 1227–1234.

———, AND L. UMLAUF. 2002. Internal gravity wave frequencies and wavenumbers from single point measurements over a slope. J. Mar. Res. **60:** 699–723.

UMLAUF, L., AND H. BURCHARD. 2003. A generic length-scale equation for geophysical turbulence model. J. Mar. Res. **61:** 235–265.

———, AND ———. 2005. Second-order turbulence closure models for geophysical boundary layers. A review of recent work. Continental Shelf Res. **25:** 795–827.

———, Y. WANG, AND K. HUTTER. 1999. Comparing two topography-following primitive equation models for lake circulation. J. Comp. Phys. **153:** 638–659.

———, ———, AND ———. 2003. Extending the k-ω turbulence model towards oceanic applications. Ocean Model. **5:** 195–218.

WAGNER, G., AND H. J. KRUSE. 1995. Analysis of the near-bottom oxygen minimum in upper Lake Constance via statistical approach. Limnologica **25:** 11–20.

WILCOX, D. C. 1998. Turbulence modelling for CFD. 2nd ed. DCW Industries, Inc.

WÜEST, A., AND A. LORKE. 2003. Small-scale hydrodynamics in lakes. Annu. Rev. Fluid Mech. **35:** 373–412. doi:10.1146/annurev.fluid.35.101101.161220.

Received: 16 July 2004
Accepted: 17 March 2005
Amended: 26 April 2005